LETTER • OPEN ACCESS

High mobility SiMOSFETs fabricated in a full 300 mm CMOS process

To cite this article: T N Camenzind *et al* 2021 *Mater. Quantum. Technol.* **1** 041001

View the article online for updates and enhancements.

You may also like

- The hybrid topological longitudinal transmon qubit
Alec Dinerstein, Caroline S Gorham and Eugene F Dumitrescu

- Low-loss high-impedance circuit for quantum transduction between optical and microwave photons
Yuta Tsuchimoto and Martin Kroner

- Controlling photoluminescence spectra of hBN color centers by selective phonon-assisted excitation: a theoretical proposal
Daniel Groll, Thilo Hahn, Pawe Machnikowski et al.

This content was downloaded from IP address 131.152.211.81 on 11/04/2022 at 15:36

Materials for Quantum Technology

OPEN ACCESS

RECEIVED
10 June 2021

REVISED
6 December 2021

ACCEPTED FOR PUBLICATION
7 December 2021

PUBLISHED
27 December 2021

Original content from this work may be used under the terms of the Creative Commons Attribution 4.0 licence.

Any further distribution of this work must maintain attribution to the author(s) and the title of the work, journal citation and DOI.

LETTER

High mobility SiMOSFETs fabricated in a full 300 mm CMOS process

T N Camenzind[1,4], A Elsayed[2,3,4], F A Mohiyaddin[3], R Li[3], S Kubicek[2,3], J Jussot[3], P Van Dorpe[2,3], B Govoreanu[3], I Radu[3] and D M Zumbühl[1,*]

[1] Department of Physics, University of Basel, Klingelbergstrasse 82, 4056 Basel, Switzerland
[2] Department of Physics and Astronomy, KU Leuven, Celestijnenlaan 200D, B-3001 Leuven, Belgium
[3] IMEC, Kapeldreef 75, B-3001 Leuven, Belgium
[*] Author to whom any correspondence should be addressed.
[4] These authors contributed equally to this work.

E-mail: dominik.zumbuhl@unibas.ch

Keywords: quantum transport, spin quantum computing, silicon field effect transistor

Abstract

The quality of the semiconductor–barrier interface plays a pivotal role in the demonstration of high quality reproducible quantum dots for quantum information processing. In this work, we have measured SiMOSFET Hall bars on undoped Si substrates in order to investigate the device quality. For devices fabricated in a full complementary metal oxide semiconductor (CMOS) process and of very thin oxide below a thickness of 10 nm, we report a record mobility of 17.5×10^3 cm^2 V^{-1} s^{-1} indicating a high quality interface, suitable for future qubit applications. We also study the influence of gate materials on the mobilities and discuss the underlying mechanisms, giving insight into further material optimization for large scale quantum processors.

The spin of an electron in silicon has been considered as one of the most promising candidates for large-scale quantum computers, due to its long coherence time, compactness, potential to operate at relatively high temperatures, and compatibility with complementary metal oxide semiconductor (CMOS) technology for upscaling [1–3]. High fidelity single and two qubit operations have been demonstrated in academic lab-based devices [4, 5]. The scale up process to multi-qubit arrays will however entail high quality qubits in large numbers, necessitating a transition to industrial fabrication techniques [6].

While spin qubit-devices can be fabricated using semiconductor manufacturing techniques, a detailed and careful analysis on the impact of different fabrication process steps on the performance of spin qubits is crucial. Hallbar mobility is a widely used metric to characterize the MOS interface quality, which can provide valuable feedback to fabrication process optimization. In this work, we perform transport measurements on SiMOSFETs and investigate the quantum Hall effect. The gate stack for SiMOSFET is the same as that for qubit integration [7]. We extract key characteristics of the MOS gate stack such as critical density and mobility as well as transport and quantum lifetimes. Comparing the obtained results to a transport model, we identify and quantify the leading scattering terms. Additionally, we explore possible mobility limiting factors when changing the top gate material from polySi to titanium nitride (TiN).

The devices measured in this work are undoped inversion gated Hall bars fabricated in a state-of-the art 300 mm fab line [7]. The starting substrate consists of a (100) silicon wafer with a background doping $<5 \times 10^{15}$ cm^{-3}. The Hall bar top gates are defined by electron beam lithography and subsequent dry etching process, and the fanout metal pins are defined by deep UV lithography. After depositing the gate material, the whole wafer is covered with a passivation layer. In order to measure the electronic properties of the investigated samples, a positive voltage has been applied to the top gate to form a two-dimensional electron gas (2DEG) at the interface of Si and SiO_2. Throughout this work, we perform four-wire electronic transport measurements using standard lock-in techniques. Both the longitudinal and transverse Hall voltages were measured simultaneously with differential voltage amplifiers. Additionally, the current through the

© 2021 The Author(s). Published by IOP Publishing Ltd

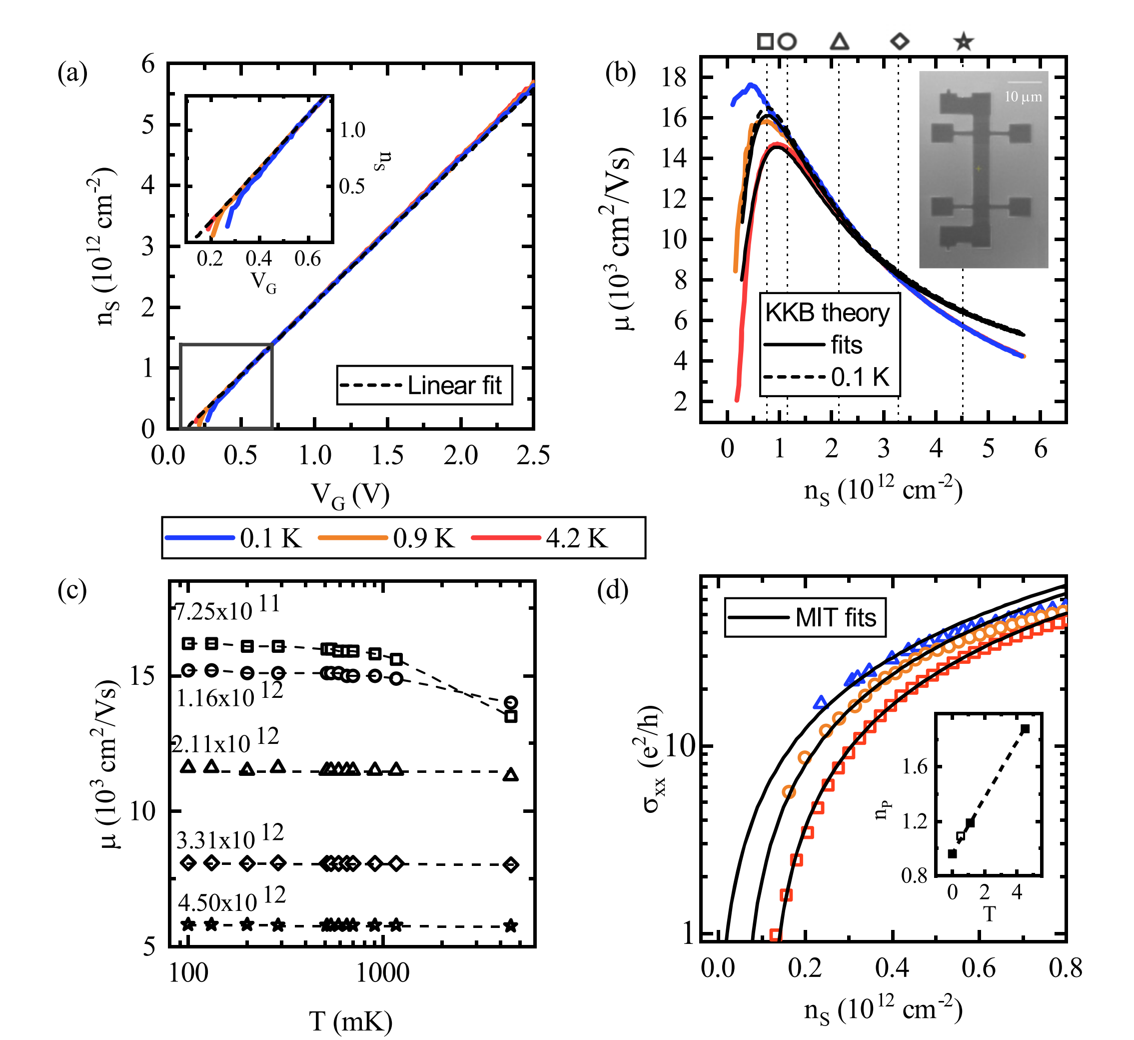

Figure 1. Density and mobility study. (a) Linear relationship between 2DEG sheet density n_S and the top gate voltage V_G. Below a top gate voltage of ≈0.4 V the extracted density deviates from the expected linear behaviour as shown in the inset. (b) Channel mobility μ measured as a function of n_S and corresponding fit to a mobility model (black) which includes scattering from charge impurities and surface roughness. The inset shows a SEM image of a similar device as the one used during the experiments with the same dimensions. (c) Channel mobility μ trends with respect to temperature at various sheet densities. The symbols coincide with the ones used in panel (b). The dashed lines are linear fits to the extracted mobilities and appear curved due to the logarithmic scale. (d) Longitudinal conductivity σ_{xx} in the low density range and fit to a percolation theory (black). A linear trend with respect to temperature for n_p is observed in the inset.

sample was measured using an IV transimpedance amplifier. The measurements were carried out in a dilution refrigerator with a base temperature of 20 mK with a 9 T magnet. Higher temperatures were achieved by heating the mixing chamber, resulting in electron temperatures between 100 mK and 4.2 K.

Figure 1 shows the density and mobility study performed on a sample with a polySi top gate at three different temperatures and on four different samples across the wafer. First, the density of charge carriers in the 2DEG was extracted from the transverse Hall effect in the linear regime far from quantum oscillations, particularly at the lowest temperature with magnetic field between ±1 T. The density of charge carriers in the 2DEG has an overall linear dependence on the applied top gate voltage V_G as expected from a plate-capacitor model. Assuming the relative dielectric constant $\epsilon_r(SiO_2) = 3.9$, we extract the thickness of the oxide and obtain a value of 8.1 ± 0.1 nm. This in good agreement with the oxide thickness of 8 nm defined during the fabrication process. As one can see in the inset of figure 1(a), the extracted density deviates from a linear regime at very low V_G near the threshold voltage, particularly at the lowest temperature. A temperature dependent dielectric constant would result in a temperature dependent slope of the n_S regardless of the V_G [8], which is not observed in this study. Partial localization of charge carriers in the disorder potential at low sheet density, on the other hand, could explain this [9]. Here, the disorder potential is mainly due to bulk charge scattering and scattering from oxide charges. At these rather low densities close to the 2D metal to insulator transition (MIT), partial localization would effectively reduce the sheet density of mobile carriers below a simple capacitor model, as observed, and thus slightly enhance the mobility, which is inversely proportional to the density.

The extracted densities, in combination with the sheet conductance from the longitudinal voltage measurements, allow for the calculation of the mobility μ at various temperatures. The resulting curves are shown in figure 1(b). We measured a maximum mobility of 17.5×10^3 cm^2 V^{-1} s^{-1}, the highest mobility reported for SiMOSFET devices with sub 10 nm oxide thickness [10–12] corresponding to a mean free path of 160 nm. The mobility is consistent in the four Hallbars measured across the wafer. Of course, we note that without the restriction of oxide thickness, much higher mobilities have been reported [13, 14]. We fit the mobility curve with the Kruithof–Klapwijk–Bakker (KKB) model (reference [15]) which includes remote impurity scattering and surface roughness terms [15, 16]. Solving the model self-consistently for three separate temperatures (0.5, 0.9 and 4.2 K) yields the charged impurity center density $N_C = 1.53 \pm 0.03 \times 10^{10}$ cm^{-2}, the rms height of the amplitude of the interface roughness $\Delta = 5.9 \pm 0.51$ Å and the correlation length $L = 1.8 \pm 0.35$ nm. The parameters extracted from the KKB model compared to other experimental studies [12, 17, 18] indicate a slightly lower charged impurity density and a larger correlation length resulting in an overall improved mobility. Lower charged impurities and a smoother interface are critical for future qubit implementations.

As shown in figure 1(b), there is a slight deviation of the maximum mobility from the theory curve at 0.9 K, and the theoretical curve does not agree with the reported data for 0.1 K in the low density regime. This could be explained by the assumption of a linear relationship between mobility and temperature in the KKB theory. According to our fitting, this assumption seems to be only valid above 1 K and can become a more complex function of temperature below 1 K if the low density regime becomes non-linear. This is due to the fact that the slightly reduced density (compared to the capacitor model) results in a slightly higher mobility, explaining the deviation of our data from the theory. Furthermore, for sheet densities n_S close to the depletion charge density n_{dep}, the calculation of the finite extent of the wave function in the KKB theory can become unreliable because of the assumed approximations. While the density in our sample is approaching a localized regime, the reported maximum mobility is at a sheet density 0.5×10^{11} cm^{-2} which corresponds to a top gate voltage of 0.4 V. At this voltage the deviation of the sheet density from the linear capacitor model is not significant (roughly 8%). The effect on the mobility is also insignificant as is confirmed when the mobility is calculated using a linearly extrapolated density (figure A1). The theoretically predicted curve can be recovered by using a linearly extrapolated density during the calculation of the mobility. Further details are discussed in appendix A. Additionally, the localization of charges is strongly suppressed with temperature. At 0.9 K the deviation from the parallel plate model is minimal and the extracted mobility fits the KKB model perfectly.

Another key parameter is the percolation density, which indicates the minimum density required to form a conducting channel. Generally, the percolation density describes the disorder in the channel at low densities, where quantum devices typically operate. In figure 1(d), we employed a MIT model in order to fit the density-dependent conductivity $\sigma_{xx} \sim (n - n_p)^p$ [17], where n_p and p are the percolation density and universal exponent, respectively. However, this model is only valid in the low density regime and deviates above $n = 8 \times 10^{11}$ cm^{-2}. We fixed the exponent $p = 1.31$, as expected in a two-dimensional system, and allowed n_p to vary [17]. Our fits yield $n_p = 1.86 \times 10^{11}$ cm^{-2} at $T = 4.2$ K. As seen in the inset of 1(d) the extracted n_p decreases with decreasing temperature, which is in agreement with previous studies [17], and is below 1×10^{11} cm^{-2} at the lowest temperature. Such a low percolation density is among the lowest reported for similar devices [12, 18].

Additionally, we investigate the temperature dependence of mobility at various top gate voltages. For sheet densities less than 2×10^{12} cm^{-2} the mobility is a function of temperature, with a linear dependence for temperatures above 1 K (see figure 1(c)). The temperature dependence of the mobility is only visible for low electron densities because mobilities at higher densities are limited by surface roughness, which is not temperature dependent. Additionally, the peak mobility shifts to higher densities at higher temperatures due to the activation of background charges limiting the mobility at high temperatures.

In order to extract more information about the transport properties and the dominating scattering mechanism, we investigated the transverse resistance R_{xy} and longitudinal resistivity ρ_{xx} in the quantum Hall regime. The magnetic field B was swept up to 8.5 T at a fixed sheet density of 7.1×10^{11} cm^{-2} near the peak mobility. As shown in figure 2(a), we observe Shubnikov–De Haas (SdH) oscillations starting at 0.8 T and begin to resolve spin splitting at 3.2 T. The ρ_{xx} shows well developed zeros for magnetic fields larger than 3.8 T. In combination with the single frequency of the SdH oscillations extracted below 2.5 T and the absence of beatings strongly indicate single subband occupancy. We further observe a four-fold degeneracy in the filling factor which changes to a two-fold degeneracy as we increased the magnetic field (figure 2(b)). The remaining two-fold degeneracy is due to the two lowest lying valleys which are split off from the remaining four valleys due to the z-confinement in silicon (100) [19]. A linear fit of the filling factor (figure 2(b)) with respect to inverse magnetic field yields a sheet density 7.1×10^{11} cm^{-2} in agreement with the extracted Hall density, further confirming clean single subband transport in the investigated samples.

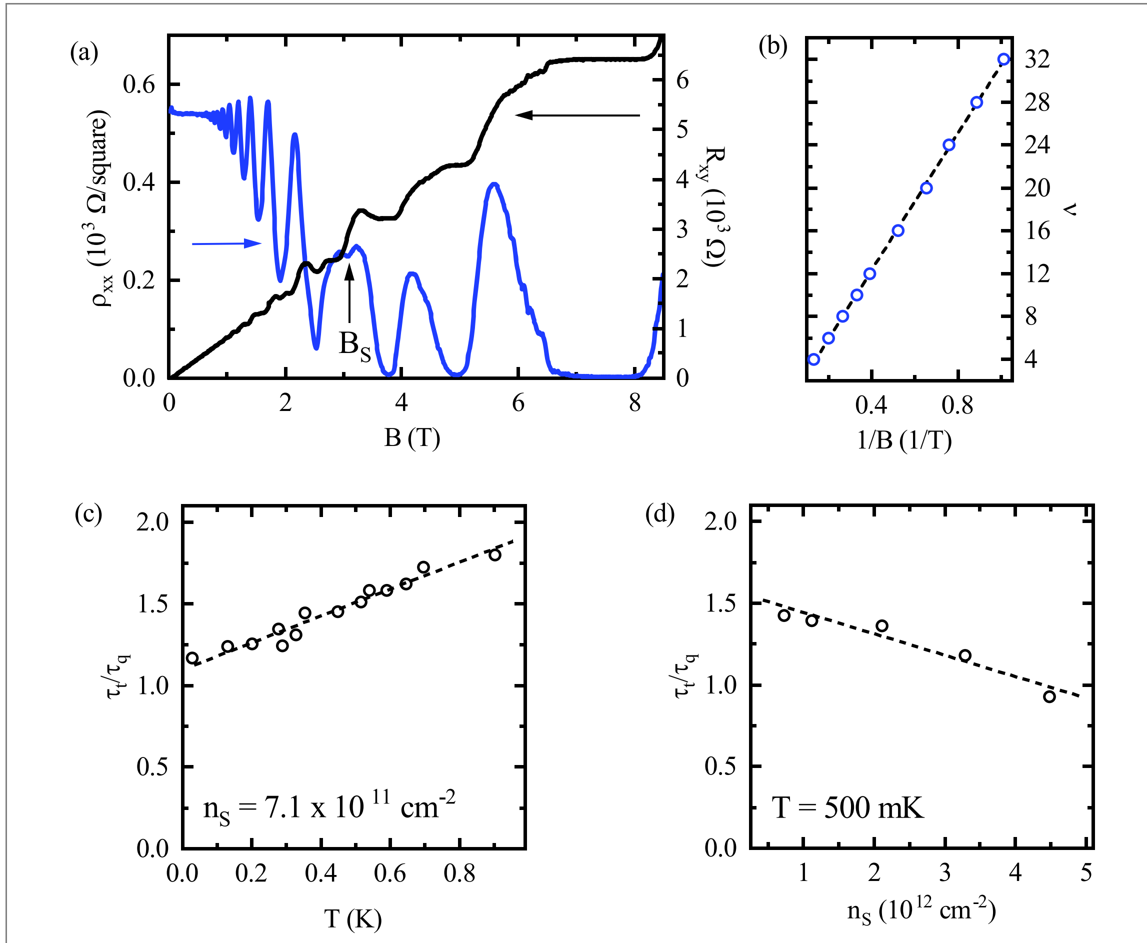

Figure 2. Extended Hall studies with transport properties. (a) Longitudinal resistivity ρ_{xx} (blue) and transverse resistance R_{xy} (black) at $n_S = 7.1 \times 10^{11}$ cm^{-2} as a function of magnetic field B. The arrow indicates the magnetic field spin is resolved. (b) Linear relationship between filling factor ν (blue scatter) and inverse magnetic field. The solid line is a fit from which the sheet density is calculated. (c) and (d) Extracted dingle ratio τ_t/τ_q as a function of temperature T and sheet density n_S, respectively. The dingle ratio is slightly temperature and density dependent and is ≈1, which indicates that large angle scattering is most dominant scattering mechanism in this sample.

Upon further investigations into the SdH oscillation amplitudes below 2.5 T, we were able to extract an effective mass $m^* = 0.21 \pm 0.02 \cdot m_0$ from the temperature dependent data, which corresponds to the transverse mass expected for silicon samples with similar background doping [20]. Further details are discussed in appendix B. From fitting the SdH envelope as a function of temperature and density, we can extract the quantum lifetime τ_q. By combining τ_q, which includes all possible scattering events, and the transport lifetime $\tau_t = e^*\mu/m^*$, which includes only the large angle scattering, we extract the so-called Dingle ratio τ_t/τ_q. The Dingle ratio thus characterizes the dominant scattering mechanism ranging from a ratio of 1 for predominant large angle scattering to values $\gg 1$ for dominant small angle scattering. Figure 2(c) shows an increase of the Dingle ratio from ≈1 to ≈2 with increasing temperature, indicating a shift in the type of scattering dominating at different temperature ranges. We can see an inverted trend for the Dingle ratio with respect to density. For a fixed temperature of 0.5 K, we observe a decrease from a ratio of ≈1.5 to ≈1 by increasing the density, again showing a slight shift towards large angle scattering. This is true for all measured temperatures and densities. In all, the observed Dingle ratio around 1 to 2 shows that short range/large angle scattering is the dominant scattering mechanism in this system, where the scattering centers are near or in the channel itself [20].

Furthermore, we investigate the effect of two different gate metals on the mobility and percolation density. We chose polySi and TiN as top gate materials since both are widely applied gating materials for integrated CMOS device fabrication. While polySi has generally larger mobilities, which indicates a small disorder potential and therefore a low dot-to-dot variation, TiN exhibits low resistivity and is superconducting at low temperatures, which is desirable for microwave qubit control and readout. The density dependent mobilities at 4.2 K, for both TiN and polySi are shown in figure 3(a). There is a decrease by a factor of three in the maximum mobility when changing the material from polySi to TiN while all other parameters in the fabrication remain the same. We expect the TiN gate to be superconducting at these temperatures and for fields lower than ∼3.3 T. However, the decrease in the mobility cannot be attributed to the modification of the magnetic

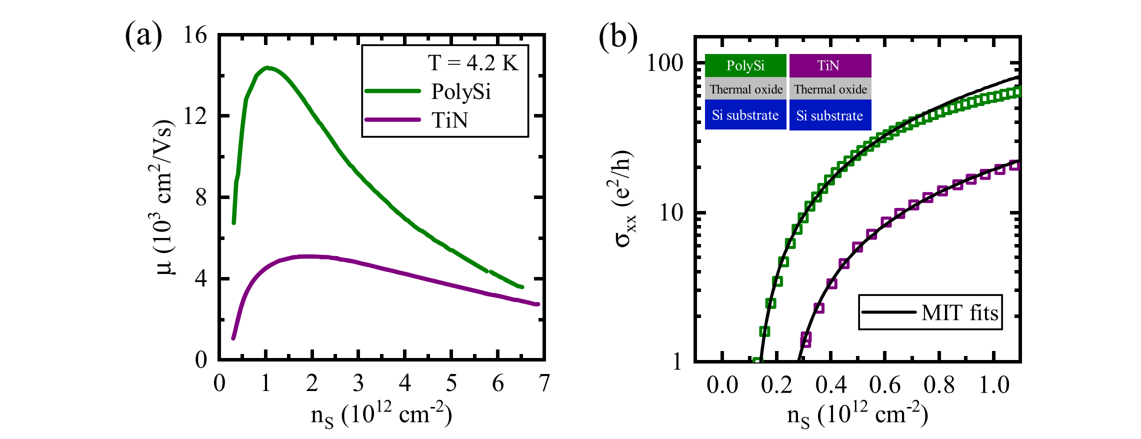

Figure 3. Gate material study. (a) The channel mobility μ with respect to sheet density n_S for polySi (green) and TiN (violet), both at 4.2 K. The mobility shows a decrease by a factor of three when changing the top gate material from polySi to TiN. (b) Longitudinal conductivity σ_{xx} with respect to sheet density. The fits to percolation theory (black) show a significant difference between the polySi and TiN percolation densities.

flux in the 2DEG due to the Meissner effect. The deposited TiN gate thickness is less than the London penetration depth λ_L, and additionally there are no discontinuities during the magnetic field sweep indicating no superconducting transition. To investigate the underlying mechanism for the mobility difference, we perform high magnetic field Hall measurements on the TiN devices as well. Unlike polySi which shows vanishing ρ_{xx} in figure 2(a), ρ_{xx} of TiN does not have well developed zeros. This can be attributed to the lower mobility and could be due to multiple subband transport [21] (see appendix C for further details). At high electron concentrations and in the presence of compressive stress, multiple subbands can be occupied and thus introduce inter-subband scattering at low temperatures.

To explain the inter-subband scattering, we firstly consider the effect of strain. On silicon (100) surfaces, materials used as top gates with certain coefficient of thermal expansion (CTE) introduce compressive strain [22]. This leads to a decrease in the energy splitting of two subsequent subbands [20, 23, 24]. Strain simulations, described in appendix D, indicate a large difference in strain between TiN and polySi. However, the strain could only decrease the TiN mobility by roughly 10 percent rather than the three fold decrease observed [24]. This difference could be explained by the oxygen scavenging of TiN on SiO_2 [25]. When depositing TiN on a SiO_2 surface, SiO_2 gets reduced to SiO_x and the free oxygen combines with TiN to form TiO_2 and titanium oxynitride (TiN_xO_y). This process creates charged oxygen vacancies in the SiO_2 layer and because the oxide is very thin in these samples, the charge carriers can then scatter at these defects thus reducing the overall mobility. Indeed, fits of the KKB model to the TiN data indicate a significantly higher N_C than polySi consistent with the scavenging hypothesis. Those two effects combined therefore could explain the difference in mobilities between the two gate metals. While TiN is desirable gate metal due to its connection the CMOS industry and superconductivity at low temperatures, the lower mobility and higher percolation density compared to polySi could potentially degrade the quality of the fabricated quantum dots. To overcome this hurdle, we can increase the oxide thickness to alleviate the effect of strain in the channel [26]. Additionally, the oxidation of the TiN can be inhibited using a high-K dielectric [25].

In summary, we have characterized SiMOSFET samples using Hall effect measurements. We found a record mobility of 17.5×10^3 cm^2 V^{-1} s^{-1} which is the highest reported mobility to date for SiMOSFET samples with sub-10 nm oxide thickness. Further, we have shown that the dominant mobility limiting factor are charges near the conducting channel, which can be improved by further reducing the impurity levels in the substrate. For example, an epitaxial layer can reach a background doping level of roughly 1×10^{12} cm^{-3}, which is three orders of magnitude lower than the samples measured in this study. Additionally, we show that the choice of top gate material directly affects the mobility and percolation density. Factors such as strain and oxygen scavenging could explain the strong influence on both parameters. This demonstrates that the choice of top gate material is of paramount importance. The MOS interface has been widely identified as the source for charge noise and disorder sites, which limits the qubit performance and upscaling.

Further improvements in mobility can be achieved by reducing charged impurity density or step height. This can be realised by additional forming gas anneals [18] or growing epitaxial pure silicon on the standard substrate. While increasing the correlation length increases high density mobility and improves device uniformity over large scale qubit arrays. Furthermore, to improve the qubit device fabrication, more systematical investigations are needed. The Hallbar mobility and the analysis presented in this study could provide valuable insight into the gate stack over a large device area and direct further fabrication optimizations, which could

pave the way for a large scale spin qubit processor integration with a full CMOS process. Spin qubits in silicon MOS structures are designed to have an effective dot diameter of roughly 10 nm. Considering spin qubits being operated in the last electron regime, we use the percolation density to estimate an approximate distance between scattering centers $\propto 1/\sqrt{n_c} \sim 35$ nm. This would, statistically, correspond to one out of every three dots having an impurity within its diameter. These estimations further highlight the importance of improving both the mobility and percolation density for spin qubit applications.

Acknowledgments

This work was performed as part of IMEC's Industrial Affiliation Program (IIAP) on Quantum Computing. Additionally, this work was supported by the Swiss Nanoscience Institute (SNI), the Swiss National Science Foundation (SNF), the National Centers of Competence in Research (NCCR) SPIN and the EU H2020 European Microkelvin Platform (EMP) Grant No. 824109.

Author contributions

TNC, AE and DMZ performed the experiments, analysed the measurements and wrote the manuscript with input from all authors. BG designed the test structures. SK and JJ fabricated the devices. FAM performed the strain simulations. The work was completed with assistance from RL, PVD and IR.

Data availability statement

The data that support the findings of this study are openly available at the zenodo repository at DOI https://doi.org/10.5281/zenodo.5762556.

Appendix A. Mobility as a function of linear density and MIT fitting range

During the calculation of the mobility at the lowest temperature, we observed a peak mobility higher than the KKB model (see figure 1(b)). We associated this deviation to the non-linear density dependence in the small top gate voltage regime at the lowest temperature as shown in the inset of figure 1(a). This assumption is further supported because the theoretical curve can be recovered using a linear extrapolated density when calculating the mobility (see figure A1). This behaviour can be explained within the KKB theory, where the depletion charge density n_{dep} is implicitly assumed to be significantly smaller than the sheet density n_{S} especially in the critical regime of maximum mobility [15]. If the density becomes non-linear, this violation of the linear density assumption has a significant impact when calculating the finite extent of the wave function b within the Coulomb scattering term $\langle |U_{\mathrm{C}}(q)|^2 \rangle$ and the dielectric response function ε. Further research in this regime is needed in order to capture the behaviour found in this work, but it exceeds the scope of this work. Nevertheless, we emphasize the mobility of 17.5×10^3 cm^2 V^{-1} s^{-1} is the properly measured mobility, and the slightly lower peak mobility of 16.5×10^3 cm^2 V^{-1} s^{-1} in figure A1 is a modelled mobility assuming a linear density model. The previous mobility record was $\approx 10 \times 10^3$ cm^2 V^{-1} s^{-1} for a comparable sample although the oxide was slightly thicker in that work [12].

The MIT model we used in this work is only valid at very low densities (below 1×10^{12} cm^{-2}) and therefore is rather sensitive to the fitting range. In order to find the appropriate fitting range, we varied both the minimum and maximum value independently. As shown in figure A1, we determined that fitting the data between 2.7×10^{11} cm^{-2} and 6.0×10^{11} cm^{-2} yields the most reliable outcome because variations in the fitting range do not significantly change the result.

Appendix B. Extraction of m^* and τ_{q}

In order validate our evaluation approach and our experiments, we extract the effective mass from the temperature dependence of the SdH oscillations as seen in figure B1. For that, we subtract a polynominal background from the ρ_{xx} data and use the following formula as described in [27, 28]

$$\frac{\Delta\rho_{xx}(T)}{\Delta\rho_{xx}(T_0)} = \frac{T}{T_0} \cdot \frac{\sinh\,\chi(T)}{\sinh\,\chi(T_0)} \tag{B.1}$$

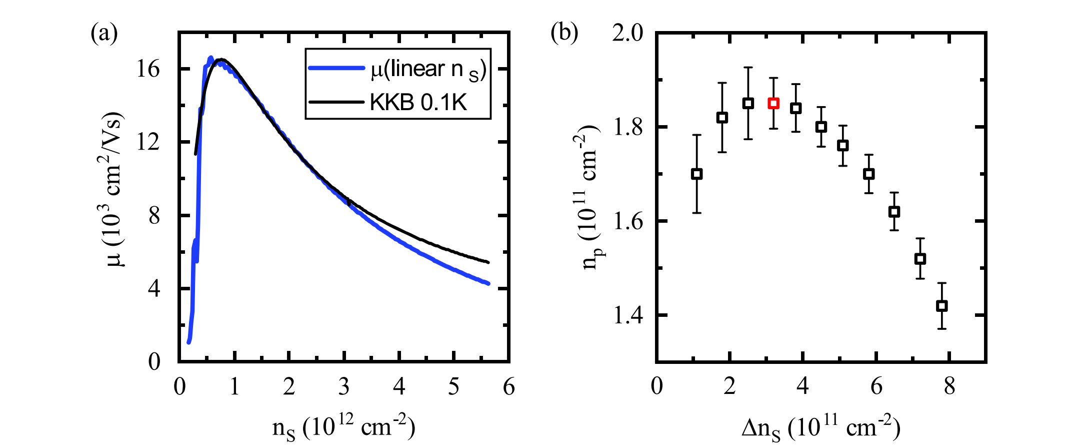

Figure A1. Mobility as a function of linear density and MIT fitting range. (a) When using a linearly extrapolated (instead of the carefully extracted) density in order to calculate the mobility of our sample (blue), the peak mobility becomes slightly smaller than previously demonstrated in figure 1(b). Additionally, we can fit the KKB theory (black) self-consistently with the other temperature data highlighting the importance of the density values. (b) By varying Δn_S for extracting the percolation density n_p within the MIT model, we determine the optimal fitting range. We chose $\Delta n_S = 3.2 \times 10^{11}$ cm^{-2} (indicated by the red box) because the extracted n_p does not change significantly while changing Δn_S.

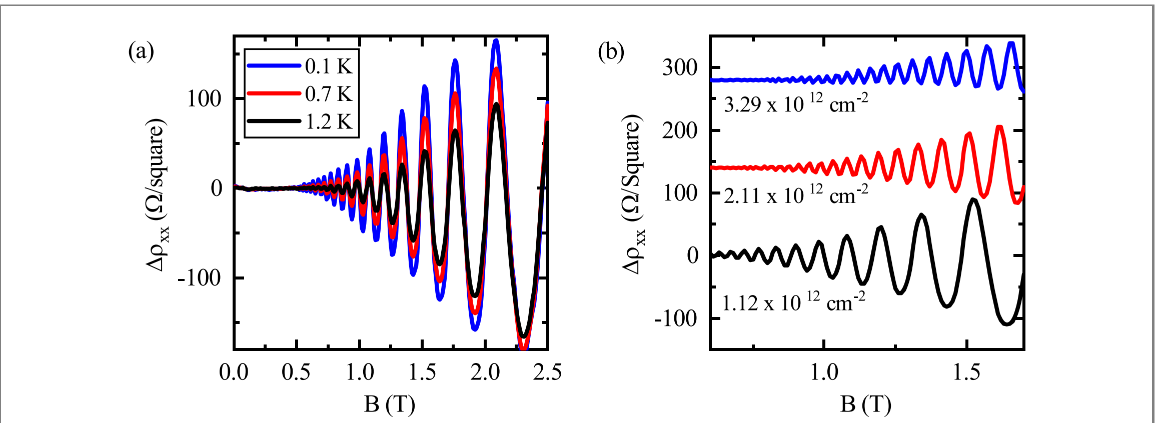

Figure B1. SdH oscillations. (a) We can extract the effective mass by analysing the temperature dependent SdH oscillations at various magnetic field values B. (b) The envelope of the SdH oscillations in the fully spin and valley degenerate regime ($<$ 2.5 T) we can extract the quantum lifetime τ_q for various densities. Curves are offset for clarity.

with $\chi(T) = 2\pi^2 k_B T/\hbar\omega_c$ and $\omega_c = eB/m^*$. Here, T is the temperature, T_0 the lowest temperature, k_B is the Boltzmann constant, $\hbar$ the reduced Plank constant, e the electric charge, B the magnetic field and m^* the effective mass. Using the effective mass as the only free fit parameter, we extracted $m^* = 0.21 \pm 0.02 \cdot m_0$, which is close to the expected value of $m^* = 0.19 \cdot m_e$.

Further, the envelope of the SdH oscillations allows for the extraction of the quantum lifetime τ_q. For that, we use the following formula

$$\ln\left(\frac{\Delta\rho_{xx}(B)\sinh\chi}{\chi}\right) = C - \frac{\pi m^*}{eB\tau_q}. \quad \text{(B.2)}$$

Therefore, by analysing the slope of the magnetic field dependent logarithmic term we can extract τ_q for all measured densities and temperatures. In combination with the transport lifetime τ_t we can then further extract the dingle ratio as described in the main text.

Appendix C. TiN data at high fields

In comparison to the reported data in figure 2(a), TiN does not show well developed zeroes in the longitudinal resistivity ρ_{xx} at high magnetic fields at a temperature of 500 mK (see figure C1), as expected for a much lower mobility. Further, the transversal Hall resistance R_{xy} shows oscillating features instead of the expected Hall plateaus. This could be due to multiple subbands contributing to the overall transport or with the increased density of background charges due to the above mentioned oxygen scavenging.

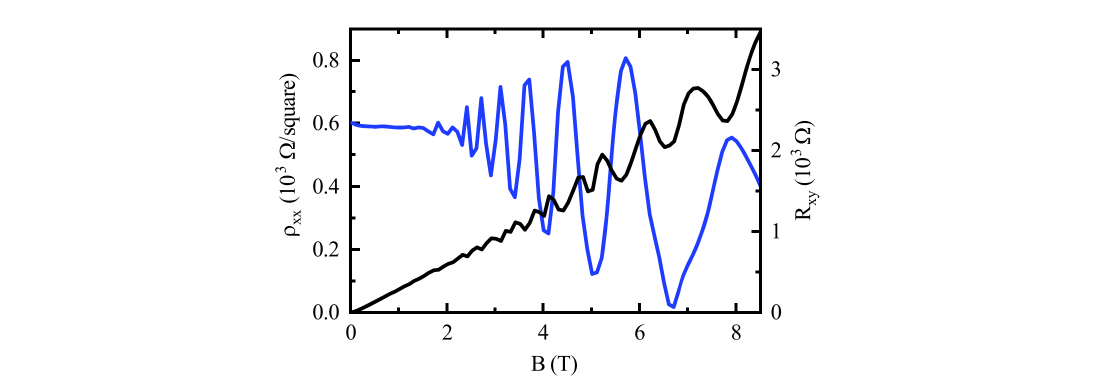

Figure C1. TiN data at high fields. Longitudinal resistivity ρ_{xx} (blue) and transverse Hall resistance R_{xy} (black) of the sample measured with a TiN top gate at 500 mK. Both the not well developed zeroes in ρ_{xx} and the oscillating R_{xy} indicate multiple subband occupancy.

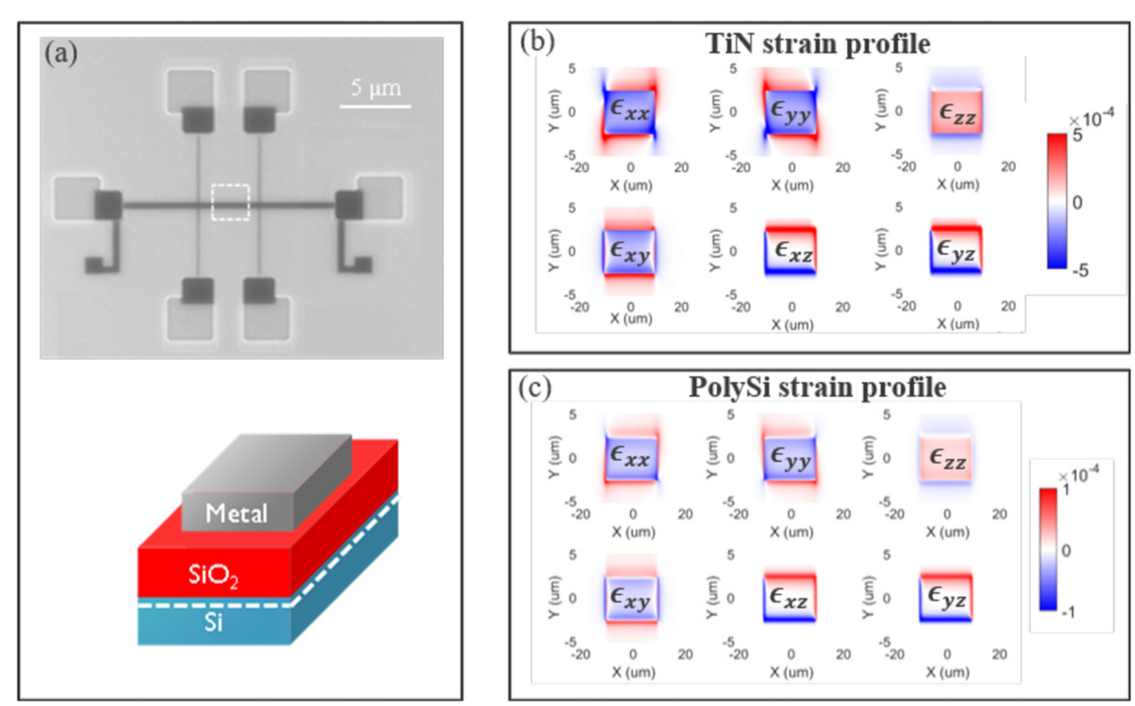

Figure D1. Gate material strain simulations. (a) Schematic of the Hall bar used for the strain simulation. The strain in the channel was calculated using sprocess in the region indicated by the dashed white line. (b) and (c) The strain in the channel for the polySi and TiN respectively. The model uses literature values for the thermal expansion coefficient for both materials.

Appendix D. Strain simulations

We quantify the stain induced in the 2DEG due to the different thermal expansion coefficients of both gate materials. The strain was simulated using a commercially available software [29]. The silicon was simulated isotropically. The temperature dependence of the CTE for polySi up to room temperature is assumed to be linear because there is no reported data above 200 K [30]. Further, we neglect the intrinsic strain induced during the fabrication process, which is beyond the scope of this work. Thermal contraction is considered from room temperature down to the cryogenic measurement temperatures. All simulations were performed in three dimensions and the components of strain $\epsilon_x, \epsilon_y, \epsilon_z$ are calculated 5 nm below the oxide due to the finite extension of the wavefunction. As shown in figures D1(b) and (c), there is a large difference in strain between TiN and polySi. While TiN induces strain up to 2.4×10^{-4}, polySi induces significantly less strain of approximately only 0.28×10^{-4}.

ORCID iDs

T N Camenzind https://orcid.org/0000-0001-6326-5717
D M Zumbühl https://orcid.org/0000-0001-5831-633X

References

[1] Vandersypen L, Bluhm H, Clarke J, Dzurak A, Ishihara R, Morello A, Reilly D, Schreiber L and Veldhorst M 2017 *npj Quantum Inf.* **3** 1–10
[2] Petta J R, Johnson A C, Taylor J M, Laird E A, Yacoby A, Lukin M D, Marcus C M, Hanson M P and Gossard A C 2005 *Science* **309** 2180–4
[3] Veldhorst M *et al* 2014 *Nat. Nanotechnol.* **9** 981–5
[4] Maurand R *et al* 2016 *Nat. Commun.* **7** 1–6
[5] Veldhorst M *et al* 2015 *Nature* **526** 410–4
[6] Li R *et al* 2018 *Sci. Adv.* **4** eaar3960
[7] Li R *et al* 2020 A flexible 300 mm integrated Si MOS platform for electron- and hole-spinqubits exploration *2020 IEEE Int. Electron Devices Meeting (IEDM)* (IEEE) pp 38–3
[8] Lautenschlager P, Garriga M, Vina L and Cardona M 1987 *Phys. Rev.* B **36** 4821
[9] Tsukada M 1976 *J. Phys. Soc. Japan* **41** 1466–72
[10] Shankar S, Tyryshkin A M, He J and Lyon S A 2010 *Phys. Rev.* B **82** 195323
[11] Rochette S *et al* 2019 *Appl. Phys. Lett.* **114** 083101
[12] Sabbagh D *et al* 2019 *Phys. Rev. Appl.* **12** 014013
[13] Kravchenko S V, Mason W, Furneaux J E and Pudalov V M 1995 *Phys. Rev. Lett.* **75** 910
[14] Popović D, Fowler A and Washburn S 1997 *Phys. Rev. Lett.* **79** 1543
[15] Kruithof G H, Klapwijk T M and Bakker S 1991 *Phys. Rev.* B **43** 6642
[16] Gold A and Dolgopolov V T 1986 *Phys. Rev.* B **33** 1076
[17] Tracy L A, Hwang E H, Eng K, Ten Eyck G A, Nordberg E P, Childs K, Carroll M S, Lilly M P and Das Sarma S 2009 *Phys. Rev.* B **79** 235307
[18] Kim J-S, Tyryshkin A M and Lyon S A 2017 *Appl. Phys. Lett.* **110** 123505
[19] Herman F 1955 *Proc. IRE* **43** 1703–32
[20] Ando T, Fowler A B and Stern F 1982 *Rev. Mod. Phys.* **54** 437
[21] Kruithof G H and Klapwijk T M 1990 *Phys. Rev.* B **42** 11412
[22] Nix F C and MacNair D 1941 *Phys. Rev.* **60** 597
[23] Kawaji S, Hatanaka K, Nakamura K and Onga S 1976 *J. Phys. Soc. Japan* **41** 1073–4
[24] Eisele I 1978 *Surf. Sci.* **73** 315–37
[25] Filatova E O, Sakhonenkov S S, Konashuk A S, Kasatikov S A and Afanas'ev V V 2019 *J. Phys. Chem.* C **123** 22335–44
[26] Mohiyaddin F A *et al* 2019 Multiphysics simulation & design of silicon quantum dot qubit devices *2019 IEEE Int. Electron Devices Meeting (IEDM)* (IEEE) pp 39–5
[27] Bauer G and Kahlert H 1972 *Phys. Rev.* B **5** 566
[28] Celik O, Tiras E, Ardali S, Lisesivdin S B and Ozbay E 2011 *Phys. Status Solidi c* **8** 1625–8
[29] Sentaurus process—technology computer aided design (tcad)—synopsys https://synopsys.com/silicon/tcad/process-simulation/sentaurus-process.html
[30] Thorbeck T and Zimmerman N M 2015 *AIP Adv.* **5** 087107